J. Fluid Mech. (2009), *vol.* 635, *pp.* 1–26.
doi:10.1017/S0022112009007551

Numerical simulation of Faraday waves

NICOLAS PÉRINET[1], DAMIR JURIC[2]
AND LAURETTE S. TUCKERMAN[1]†

[1]Laboratoire de Physique et Mécanique des Milieux Hétérogènes (PMMH), Ecole Supérieure de Physique et de Chimie Industrielles de la Ville de Paris (ESPCI), Centre National de la Recherche Scientifique (CNRS), UMR 7636, Université Paris 6 et Paris 7, 10 rue Vauquelin, 75231 Paris Cedex 5, France

[2]Laboratoire d'Informatique pour la Mécanique et les Sciences de l'Ingénieur (LIMSI), Centre National de la Recherche Scientifique (CNRS), UPR 3251, BP133, 91403 Orsay Cedex, France

(Received 31 December 2008; revised 2 April 2009; accepted 2 April 2009)

We simulate numerically the full dynamics of Faraday waves in three dimensions for two incompressible and immiscible viscous fluids. The Navier–Stokes equations are solved using a finite-difference projection method coupled with a front-tracking method for the interface between the two fluids. The critical accelerations and wavenumbers, as well as the temporal behaviour at onset are compared with the results of the linear Floquet analysis of Kumar & Tuckerman (*J. Fluid Mech.*, vol. 279, 1994, p. 49). The finite-amplitude results are compared with the experiments of Kityk *et al.* (*Phys. Rev.* E, vol. 72, 2005, p. 036209). In particular, we reproduce the detailed spatio-temporal spectrum of both square and hexagonal patterns within experimental uncertainty. We present the first calculations of a three-dimensional velocity field arising from the Faraday instability for a hexagonal pattern as it varies over its oscillation period.

1. Historical introduction

The Faraday experiment consists of shaking vertically a container holding two immiscible fluids (the lighter of which can be air) thereby inducing oscillations of the fluids and the interface between them. Beyond a certain threshold, the interface can form many kinds of standing wave patterns, including crystalline patterns and others which are more complex. This phenomenon was first studied by Faraday (1831) who noticed that the vibration frequency of the interface was half that of the forcing. The results of Faraday were confirmed by Rayleigh (1883*a*, *b*). Benjamin & Ursell (1954) carried out the first theoretical linear analysis of the Faraday waves, restricted to inviscid fluids. They decomposed the fluid motion into normal modes of the container and showed that the evolution equation of each mode reduced to a Mathieu equation whose stability diagram is well known.

In the 1990s, new behaviours of the interface were discovered, such as quasi-crystalline eight-fold patterns seen by Christiansen, Alstrøm & Levinsen (1992). By introducing a forcing which is the sum of two periodic functions with commensurable frequencies, Edwards & Fauve (1994) were able to produce twelve-fold quasi-patterns. Triangular patterns were observed by Müller (1993) and superlattice patterns by Kudrolli, Pier & Gollub (1998), also using two-frequency forcing. Spatio-temporal

---

† Email address for correspondence: laurette@pmmh.espci.fr

chaos was studied by Kudrolli & Gollub (1996), who also surveyed the occurrence of lattice patterns – stripes, squares or hexagons – as a function of viscosity and frequency. Binks, Westra & van de Water (1997) demonstrated the dependence of the pattern on the depth of the layer. In addition to patterns or quasi-patterns, very localized circular waves called oscillons may occur, as seen by Lioubashevski, Arbell & Fineberg (1996). The Faraday instability is the first macroscopic system in which such structures have been observed. These discoveries endow the Faraday instability with a very great fundamental interest for understanding the natural formation of patterns.

A number of theoretical or semi-numerical analyses were inspired by these experiments. Kumar & Tuckerman (1994) extended the linear stability analysis of Benjamin & Ursell (1954) to viscous fluids. This analysis was experimentally confirmed by Bechhoefer *et al.* (1995) and used by Kumar (1996) to predict cases in which the response would be harmonic rather than subharmonic. The method was extended by Besson, Edwards & Tuckerman (1996) to calculate the stability tongues in the case of two-frequency forcing. Integral equation formulations of the viscous linear stability problem were derived by Beyer & Friedrich (1995) and Müller *et al.* (1997), who also studied the harmonic response case. Cerda & Tirapegui (1998) used the lubrication approximation and the Wentzel–Kramers–Brillouin (WKB) method to study shallow viscous layers, obtaining a Mathieu equation that was later used by Huepe *et al.* (2006) to derive analytic results about the response to multifrequency forcing.

Linear analysis provides no information about the shape of the patterns which appear; other means are necessary to understand the occurrence of a given pattern or the amplitude of stabilization. Weakly nonlinear approximations have been derived from the Navier–Stokes equations by Viñals and co-workers, e.g. Zhang & Viñals (1997), Chen & Viñals (1999) and by Skeldon & Guidoboni (2007), focusing on the competition between different patterns. Vega, Knobloch & Martel (2001) derived equations governing the interaction between Faraday waves and the mean flow. There has been a great deal of analysis of lattices, superlattices and quasi-patterns using equivariant dynamical systems theory, as well as model equations designed to produce specific patterns, e.g. Porter, Topaz & Silber (2004). The approximation of quasi-patterns in spatially periodic domains has also been addressed in Rucklidge & Silber (2009).

Investigation of the full nonlinear viscous problem, however, requires numerical simulations, of which there have been very few up to now, specifically those of Chen & Wu (2000), Chen (2002), Murakami & Chikano (2001), Valha, Lewis & Kubie (2002), Ubal, Giavedoni & Saita (2003) and O'Connor (2008). With the exception of O'Connor (2008), all previous simulations have been two-dimensional. The most extensive simulation thus far has been that of Chen & Wu (2000) and Chen (2002), who used a finite-difference method applied to a boundary-fitted time-dependent coordinate system. At each time step, the surface is advected and a new two-dimensional grid, adapted to the surface, is recomputed. The amplitude of their numerically computed Faraday waves confirmed the weakly nonlinear analysis of Chen & Viñals (1999), including their prediction of a range of subcriticality. Their calculations also predicted qualitatively new phenomena, such as disconnected solution branches and slow modulated dynamics.

Murakami & Chikano (2001) used a method similar to that of Chen & Wu (2000) and Chen (2002). Although they reproduced some features of the experiments by Lioubashevski *et al.* (1996), their calculations were limited to accelerations only 0.5 % above critical. The investigation by Ubal *et al.* (2003) focused on the influence of liquid depth in two-dimensional simulations using a Galerkin finite-element method in transformed coordinates. In addition to comparing their linear stability predictions with those of Benjamin & Ursell (1954) and Kumar & Tuckerman (1994), they calculated instantaneous surface profiles and velocity fields, as well as the temporal evolution and spectrum. Valha *et al.* (2002) examined the response of a liquid layer in a vertical cylindrical vessel using the Marker-and-Cell (MAC) method of Harlow & Welch (1965). Surface tension was treated by the continuum surface force model of Brackbill, Kothe & Zemach (1992). O'Connor (2008) conducted numerical simulations using an Arbitrary Lagrangian–Eulerian (ALE) spectral-element code in both two and three dimensions; a visualization of a square pattern was presented.

The hexagonal patterns, quasi-patterns and oscillons which motivate our investigation are intrinsically three-dimensional, and have never been calculated numerically from the fluid-dynamical equations. Here we report on the results of fully nonlinear, three-dimensional simulations of Faraday waves using a finite-difference front-tracking method. In the classic Faraday problem the lighter fluid is usually taken to be air whose effects can be neglected. However, in contrast to the previously cited investigations, the numerical method described here solves the Navier–Stokes equations for the general case of two distinct superposed fluids. The capability of the method to simulate the motion of both fluids is important in that it permits comparison of numerical results with those of certain experimental configurations, namely those of Kityk *et al.* (2005) where the lighter fluid cannot be ignored. These experiments were the first to provide quantitative measurements of the complete spatio-temporal Fourier spectrum of Faraday waves and thus form an excellent basis for quantitative comparison with our numerical results in the nonlinear finite amplitude regime, i.e. interfaces with steep slopes.

In the next two sections of this article, we present the hydrodynamic equations that govern the Faraday instability and then describe the computational method. The two sections following these are dedicated to the comparison of our results with the linear theory of Kumar & Tuckerman (1994) and with the experiments of Kityk *et al.* (2005, 2009). After comparing numerical and experimental spatio-temporal spectra for squares and hexagons, we present the three-dimensional velocity field for the hexagonal pattern.

2. Equations of motion

The mathematical model of the Faraday experiment consists of two incompressible and immiscible viscous fluids in a three-dimensional domain $\boldsymbol{x}=(x,y,z)\in\Re^2\times[0,h]$, bounded at $z=0$ and $z=h$ by flat walls. The two fluids, each uniform and of densities ρ_1, ρ_2 and viscosities μ_1 and μ_2, initially form two superposed horizontal layers with an interface between them. This two-dimensional interface is defined by $\boldsymbol{x}'=(x,y,\zeta(x,y,t))$. Within the parameter range we wish to simulate, the height ζ remains a single-valued function of (x,y,t).

The container is shaken vertically in z. In the reference frame of the container the boundary conditions for the fluid velocities $\boldsymbol{u}=(u,v,w)$ are

$$\boldsymbol{u}(x,y,0,t)=0, \tag{2.1a}$$

$$\boldsymbol{u}(x,y,h,t)=0. \tag{2.1b}$$

The gravitational acceleration g is augmented by a temporally periodic inertial acceleration

$$\boldsymbol{G}=(a\cos(\omega t)-g)\boldsymbol{e}_z, \tag{2.2}$$

where a is the amplitude of the forcing and ω is its frequency.

The Navier–Stokes equations for incompressible, Newtonian fluids are

$$\rho\frac{\mathrm{D}\boldsymbol{u}}{\mathrm{D}t} = -\nabla p + \rho\boldsymbol{G} + \nabla\cdot\mu(\nabla\boldsymbol{u} + \nabla\boldsymbol{u}^{\mathrm{T}}) + \boldsymbol{s}, \tag{2.3a}$$

$$\nabla\cdot\boldsymbol{u} = 0. \tag{2.3b}$$

Here p is the pressure and $\boldsymbol{s}$ is the capillary force (per unit volume) and is defined below. Equations (2.3a) and (2.3b) are valid for the entire domain, including the interface, in spite of the fact that the density and viscosity change discontinuously and the surface tension acts only at the interface. In this single-fluid formulation, the density and viscosity fields are defined in terms of the densities and viscosities of the two fluids

$$\rho = \rho_1 + (\rho_2 - \rho_1)H, \tag{2.4a}$$

$$\mu = \mu_1 + (\mu_2 - \mu_1)H, \tag{2.4b}$$

with the aid of a Heaviside function,

$$H(\boldsymbol{x} - \boldsymbol{x}') = \begin{cases} 0 \text{ if } z < \zeta(x, y, t) \\ 1 \text{ if } z \geqslant \zeta(x, y, t) \end{cases}, \tag{2.5}$$

where we recall that $\boldsymbol{x} = (x, y, z)$ is a point anywhere in the three-dimensional volume and $\boldsymbol{x}' = (x, y, \zeta(x, y, t))$ is the vertical projection of $\boldsymbol{x}$ onto the interface. The capillary force is

$$\boldsymbol{s} = \int_{S'(t)} \sigma\kappa\, \boldsymbol{n}\, \delta(\boldsymbol{x} - \boldsymbol{x}')\, \mathrm{d}S, \tag{2.6}$$

where σ is the surface tension coefficient, assumed to be constant, $\boldsymbol{n}$ is the unit normal to the interface (directed into the upper fluid) and κ its curvature. $\delta(\boldsymbol{x} - \boldsymbol{x}')$ is a three-dimensional Dirac distribution that is non-zero only where $\boldsymbol{x} = \boldsymbol{x}'$. $S'(t)$ is the surface defined by the instantaneous position of the interface.

To complete the system of equations we need an expression for the motion of the interface. One such expression can be easily derived by noting that mass conservation in an incompressible flow requires $\mathrm{D}\rho/\mathrm{D}t = 0$, which in view of the discontinuous density field (2.4a), is equivalent to

$$\mathrm{D}H/\mathrm{D}t = 0. \tag{2.7}$$

Thus the interface is represented implicitly by H and advected by material motion of the fluid.

3. Computational methods

The computational domain is a rectangular parallelepiped, horizontally periodic in x and y and bounded in z by flat walls for which we impose no-slip boundary conditions. The entire domain is discretized by a uniform fixed three-dimensional finite-difference mesh. This mesh has a standard staggered MAC cell arrangement (Harlow & Welch 1965) where the u, v and w velocity nodes are located on the corresponding cell faces and scalar variables are located at the cell centres. Each cell is of dimension $\Delta x \times \Delta y \times \Delta z$.

Within the domain, the two distinct immiscible fluids are separated by a two-dimensional interface which is discretized by a second mesh as sketched in figure 1. This moving and deformable mesh is composed of triangular elements whose motion is treated by a front-tracking/immersed-boundary method (Peskin 1977; Tryggvason

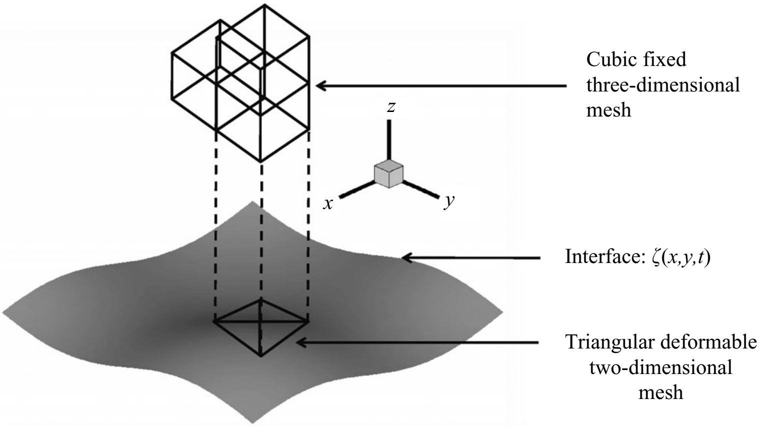

FIGURE 1. Spatial discretization of the domain.

et al. 2001). Because we have assumed that $\zeta(x, y, t)$ is single valued, the nodes of the mesh can be fixed in x and y and only their vertical displacements need to be calculated, which is a considerable simplification to the general front-tracking method.

After setting appropriate initial and boundary conditions, the computational solution algorithm for each time step is composed of three main phases. First, the interface is advected and the density and viscosity fields updated according to the new interface position. The capillary force $\boldsymbol{s}$ is then calculated. Finally, the velocity and pressure are found by means of a standard projection method. Each of these steps is described below.

3.1. *Advection of the interface*

Purely Eulerian interface methods such as Volume of Fluid (Hirt & Nichols 1981) or Level Set (Osher & Sethian 1988) use a form of (2.7) to advect a scalar field such as H, or a level-set function that implicitly represents the interface. However, in the front-tracking approach that we use here, the interface markers themselves (the nodes of the triangular mesh) are advected. H is then constructed from the position and geometry of the interface. Taking (2.7) as a starting point, we develop an equivalent expression for the vertical displacement of the triangular interface mesh.

The material derivative of (2.5) gives:

$$\frac{\mathrm{D}H}{\mathrm{D}t} = \nabla H \cdot \frac{\mathrm{D}\boldsymbol{x}}{\mathrm{D}t} + \nabla' H \cdot \frac{\mathrm{D}\boldsymbol{x}'}{\mathrm{D}t}, \tag{3.1}$$

where $\nabla' = \partial_{\boldsymbol{x}'}$ and

$$\nabla H = -\nabla' H = \int_{S'(t)} \boldsymbol{n}\delta(\boldsymbol{x} - \boldsymbol{x}')\,\mathrm{d}S. \tag{3.2}$$

(For a derivation of (3.2) see Tryggvason *et al.* 2001.) Factoring (3.1) by ∇H

$$\frac{\mathrm{D}H}{\mathrm{D}t} = \nabla H \cdot \left(\boldsymbol{u} - \frac{\mathrm{D}\boldsymbol{x}'}{\mathrm{D}t}\right). \tag{3.3}$$

The right-hand side of (3.3) can only be zero everywhere, including on the surface, $\boldsymbol{x} = \boldsymbol{x}'$, if

$$\frac{\mathrm{D}\boldsymbol{x}'}{\mathrm{D}t} = \boldsymbol{u}(\boldsymbol{x}', t), \tag{3.4}$$

which establishes the material motion of the explicit interface representation $\boldsymbol{x}'$. Furthermore

$$\frac{\partial \boldsymbol{x}'}{\partial t} = \left(\boldsymbol{I} - \nabla \boldsymbol{x}'\right) \cdot \boldsymbol{u}(\boldsymbol{x}', t), \tag{3.5}$$

where $\boldsymbol{I}$ is the identity tensor. The specific choice of $\boldsymbol{x}' = (x, y, \zeta(x, y, t))$ made here gives for $\nabla \boldsymbol{x}'$

$$\begin{bmatrix} 1 & 0 & 0 \\ 0 & 1 & 0 \\ \dfrac{\partial \zeta}{\partial x} & \dfrac{\partial \zeta}{\partial y} & 0 \end{bmatrix}. \tag{3.6}$$

With this, (3.5) leads to the specific displacement relations:

$$\partial x / \partial t = 0, \tag{3.7a}$$

$$\partial y / \partial t = 0, \tag{3.7b}$$

$$\frac{\partial \zeta}{\partial t} = w - u \frac{\partial \zeta}{\partial x} - v \frac{\partial \zeta}{\partial y}. \tag{3.7c}$$

The application of this advection to the triangular mesh we use for tracking the interface is straightforward. At each vertex the horizontal displacement is zero and for the vertical displacement we compute a first-order approximation to (3.7*c*):

$$\frac{\zeta^{n+1} - \zeta^{n}}{\Delta t} = w^{n}(\boldsymbol{x}'_e) - \frac{\partial \zeta^{n}}{\partial x} u^{n}(\boldsymbol{x}'_e) - \frac{\partial \zeta^{n}}{\partial y} v^{n}(\boldsymbol{x}'_e). \tag{3.8}$$

The superscripts n and $n+1$ denote, respectively, the old and new time levels. The derivatives on the right-hand side are evaluated using a simple upwind scheme which requires the usual Courant–Friedrichs–Lewy (CFL) time step restriction. The vertical displacement of the interface mesh requires knowledge of the velocities at the element nodes $\boldsymbol{x}'_e$. These in general do not coincide with the Eulerian grid nodes $\boldsymbol{x}_{ijk}$, whose indices correspond to discretized coordinates along the respective directions x, y and z. The problem of communicating Eulerian grid velocities to the element nodes is overcome by interpolation between the two grids as is typically done in front-tracking and immersed-boundary methods. Here we use the particular interpolation

$$\boldsymbol{u}(\boldsymbol{x}'_e) = \sum_{ijk} \boldsymbol{u}(\boldsymbol{x}_{ijk}) \delta_h(\boldsymbol{x}_{ijk} - \boldsymbol{x}'_e) \Delta x \Delta y \Delta z. \tag{3.9}$$

The kernel δ_h is a smoothed version of the three-dimensional Dirac delta function with compact support of four grid nodes in each direction (for details of the front-tracking method, see Tryggvason *et al.* 2001, and for the immersed-boundary method, see Peskin 1977). In (3.9) the weighted information collected from nearby Eulerian grid nodes is interpolated to a given element node.

We now seek to update the density and viscosity fields needed in (2.4), which require H. The equation for H, based on the updated values of $\boldsymbol{x}'$ and $\boldsymbol{n}$, is formulated by taking the divergence of (3.2):

$$\nabla^2 H = \nabla \cdot \int_{S'(t)} \boldsymbol{n}\, \delta(\boldsymbol{x} - \boldsymbol{x}')\, \mathrm{d}S, \tag{3.10a}$$

$$H(x, y, 0, t) = 0, \tag{3.10b}$$

$$H(x, y, h, t) = 1. \tag{3.10c}$$

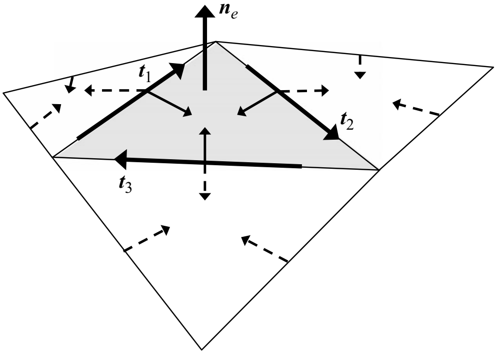

FIGURE 2. A triangular element of the interface mesh illustrating the action of the capillary forces according to (3.13). For the shaded triangle the forces act perpendicular to the triangle's edges (unlabelled solid arrows), the dashed arrows are the corresponding forces on the edges of neighbouring triangles. The net capillary force at the shared edge between any two triangles (the sum of the solid and dashed vectors) is directed into the fluid on the concave side of the interface.

The discretized version of the Poisson problem (3.10*a*) is

$$\nabla^2 H_{ijk} = \nabla \cdot \sum_e \boldsymbol{n}_e \delta_h(\boldsymbol{x}_{ijk} - \boldsymbol{x}'_e)\Delta S_e, \tag{3.11}$$

where standard central differencing is used for the gradient and divergence operators. This numerically calculated Heaviside function is a smoothed transition from 0 to 1 across a distance of 4 grid cells in the direction normal to the interface. In contrast to (3.9), the summation above serves to distribute weighted information from an element node to nearby Eulerian grid nodes. Since an element is triangular, its vertices lie in the same plane, its normal vector is unique and the three tangent vectors are simple to calculate:

$$\boldsymbol{n}_e = \frac{\boldsymbol{t}_2 \times \boldsymbol{t}_1}{\|\boldsymbol{t}_2 \times \boldsymbol{t}_1\|} \tag{3.12}$$

where $\boldsymbol{t}_1$ and $\boldsymbol{t}_2$ are the tangents on two distinct edges of the triangle (see the sketch in figure 2). We solve (3.11) by fast Fourier transform. Finally, ρ^{n+1} and μ^{n+1} are updated using (2.4*a*) and (2.4*b*).

3.2. *Capillary force*

From (2.6), the capillary force involves the curvature of the interface and its normal vector. However, from a computational point of view, curvature is a difficult quantity to compute accurately. It is more accurate and physically appealing to calculate the force pulling on the edge of each individual triangular surface element and then sum the contributions for all the elements over the surface. For a given surface element e of surface area δA and perimeter δl, we can write:

$$\begin{aligned} \boldsymbol{s}_e &= \sigma \int_{\delta A} \kappa \boldsymbol{n} \, \mathrm{d}A, \\ &= \sigma \int_{\delta A} (\boldsymbol{n} \times \nabla) \times \boldsymbol{n} \, \mathrm{d}A, \\ &= \sigma \oint_{\delta l} \boldsymbol{t} \times \boldsymbol{n} \, \mathrm{d}l, \end{aligned} \tag{3.13}$$

where the last integral represents the sum of the capillary forces exerted around the element perimeter. As sketched in figure 2, the directions of these forces are oriented along the surface and normal to the element's edges. The net force at the shared edge between any two triangles (the sum of the solid and dashed vectors) is directed into the fluid on the concave side of the interface. Following Peskin's immersed boundary method (Peskin 1977), the discrete version of (2.6) becomes

$$\boldsymbol{s}_{ijk} = \sum_e \boldsymbol{s}_e \delta_h(\boldsymbol{x}_{ijk} - \boldsymbol{x}'_e), \tag{3.14}$$

where we use the same smoothed δ_h as in (3.9) and (3.11). Thereby, several interfacial elements contribute to the calculation of the force applied to a single Eulerian node, and a single element influences more than one Eulerian node.

3.3. *Solution of the Navier–Stokes equations*

The Navier–Stokes equations are solved by a projection method (Chorin 1968; Temam 1968) with incremental pressure correction (Goda 1979) applied to a finite-difference scheme which is first order in time and second order in space. In addition a semi-implicit scheme is chosen for the velocities to relax the stability restriction on the time step due to viscous diffusion. All spatial derivative operators are evaluated using standard centred differences, except in the nonlinear term where we use a second-order Essentially-Non-Oscillatory (ENO) scheme (Shu & Osher 1989; Sussman *et al.* 1998). (For an overview of projection methods for the incompressible Navier–Stokes equations, see Guermond, Minev & Shen 2006.) The time stepping algorithm is thus

$$\begin{aligned} \frac{\boldsymbol{u}^{n+1} - \boldsymbol{u}^n}{\Delta t} = &-\boldsymbol{u}^n \cdot \nabla \boldsymbol{u}^n + \frac{1}{\rho^{n+1}} \nabla \cdot \mu^{n+1} (\nabla \boldsymbol{u} + \nabla \boldsymbol{u}^{\mathrm{T}})^{n+1} \\ &- \frac{1}{\rho^{n+1}} \nabla p^{n+1} + \frac{\boldsymbol{s}^{n+1}}{\rho^{n+1}} + \boldsymbol{G}^{\,n+1}, \end{aligned} \tag{3.15}$$

with the boundary conditions on the top and bottom walls

$$\boldsymbol{u}^{n+1}\big|_{\Gamma} = 0. \tag{3.16}$$

In (3.15), ρ, μ and $\boldsymbol{s}$ depend on $\boldsymbol{x}$ via (2.4–2.6) and have already been updated by (3.8). We decompose the solution of (3.15) in three steps. The first step is a semi-implicit calculation of an intermediate unprojected velocity $\tilde{\boldsymbol{u}}$, involving only velocities and their gradients:

$$\frac{\tilde{\boldsymbol{u}} - \boldsymbol{u}^n}{\Delta t} = -\boldsymbol{u}^n \cdot \nabla \boldsymbol{u}^n + \frac{1}{\rho^{n+1}} \nabla \cdot \mu^{n+1} (\nabla \tilde{\boldsymbol{u}} + \nabla \tilde{\boldsymbol{u}}^{\mathrm{T}}) \tag{3.17a}$$

$$\tilde{\boldsymbol{u}}|_{\Gamma} = 0 \tag{3.17b}$$

In the second step, we include the capillary, acceleration and old pressure gradient terms to calculate the unprojected velocity $\boldsymbol{u}^*$:

$$\frac{\boldsymbol{u}^* - \tilde{\boldsymbol{u}}}{\Delta t} = \boldsymbol{G}^{n+1} + \frac{\boldsymbol{s}^{n+1}}{\rho^{n+1}} - \frac{1}{\rho^{n+1}} \nabla p^n. \tag{3.18}$$

Finally we perform a projection step to find the divergence free velocity $\boldsymbol{u}^{n+1}$:

$$\frac{\boldsymbol{u}^{n+1} - \boldsymbol{u}^*}{\Delta t} = -\frac{1}{\rho^{n+1}} \nabla (p^{n+1} - p^n), \tag{3.19a}$$

$$\nabla \cdot \boldsymbol{u}^{n+1} = 0, \tag{3.19b}$$

$$\boldsymbol{u}^{n+1} \cdot \boldsymbol{n}|_{\Gamma} = 0. \tag{3.19c}$$

Equations (3.19) imply the following elliptic problem for the pressure increment

$$\frac{\nabla\cdot\boldsymbol{u}^*}{\Delta t} = \nabla\cdot\frac{1}{\rho^{n+1}}\nabla(p^{n+1}-p^n), \tag{3.20a}$$

$$\left.\frac{\partial(p^{n+1}-p^n)}{\partial\boldsymbol{n}}\right|_\Gamma = 0, \tag{3.20b}$$

which we solve with an iterative biconjugate gradient stabilized algorithm (Saad 1996). In the horizontal directions, periodic boundary conditions are imposed on the velocity and pressure, thus excluding a net horizontal pressure gradient. For the simulations we will present here, this choice is consistent with the requirement of no mean horizontal flux in a large but bounded container.

We note that in the implicit solution of (3.17), we apply the same biconjugate gradient stabilized solver used for the pressure to each component of $\tilde{\boldsymbol{u}} = (\tilde{u}, \tilde{v}, \tilde{w})$ separately. Thus only the diagonal terms of the diffusion operator are treated fully implicitly. The off-diagonal terms are treated quasi-implicitly in that the newest available values of $(\tilde{u}, \tilde{v}, \tilde{w})$ are used in the evaluation of the cross derivatives. To ensure symmetry, we permute the order of solution for each component.

4. Results: linear analysis

4.1. *Floquet analysis*

In the absence of lateral boundaries, the equations are homogeneous in the horizontal coordinates and the solutions can be represented by a spatial Fourier transform:

$$\zeta(x, y, t) = \sum_{\boldsymbol{k}} \hat{\zeta}(\boldsymbol{k}, t)\mathrm{e}^{\mathrm{i}\boldsymbol{k}\cdot\boldsymbol{x}} \tag{4.1}$$

The linear instability of the interface between two fluids is described by (2.2)–(2.7) linearized about a zero velocity field and flat interface $\zeta = \langle\zeta\rangle$. The linearized equations depend only on the wavenumber $k \equiv \|\boldsymbol{k}\|$ of each wave and not on its orientation and hence the coefficient of $\mathrm{e}^{\mathrm{i}\boldsymbol{k}\cdot\boldsymbol{x}}$ can be written as $\hat{\zeta}(k, t)$; additionally the dynamics of each $\hat{\zeta}(k, t)$ is decoupled from the others. Linear partial differential equations with constant coefficients have solutions which are exponential or trigonometric in time. For the Faraday instability, $\hat{\zeta}(k, t)$ is instead governed by a system of linear partial differential equations with time-periodic coefficients, i.e. a Floquet problem, whose solutions are of the form

$$\hat{\zeta}(k, t) = \mathrm{e}^{(\gamma+\mathrm{i}\alpha\omega)t} f(k, t \bmod T), \tag{4.2}$$

where $T = 2\pi/\omega$, γ is real and $\alpha \in [0, 1[$. The Floquet modes,

$$f(k, t \bmod T) = \sum_{n=-\infty}^{\infty} f_n(k)\mathrm{e}^{\mathrm{i}n\omega t}, \tag{4.3}$$

are not trigonometric, but remain periodic with fundamental frequency ω. Thus, the linearized behaviour for a single mode is

$$\zeta(x, y, t) = \mathrm{e}^{\mathrm{i}\boldsymbol{k}\cdot\boldsymbol{x}}\mathrm{e}^{(\gamma+\mathrm{i}\alpha\omega)t} \sum_{n=-\infty}^{\infty} f_n(k)\mathrm{e}^{\mathrm{i}n\omega t}. \tag{4.4}$$

Analogous expressions hold for the velocity $\boldsymbol{u}$.

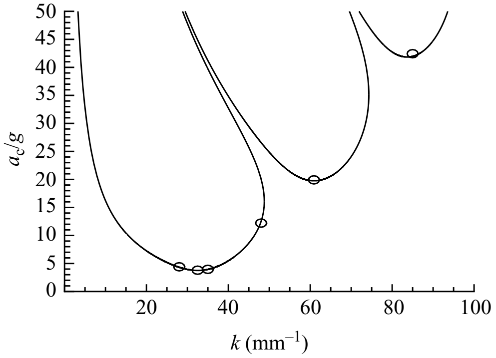

FIGURE 3. Critical acceleration a_c/g as a function of the wavenumber k. The solid curves represent the neutral curves obtained by Kumar & Tuckerman (1994). The a_c found with the simulation are indicated by the circles.

Equation (4.2) shows that if γ is non-zero or α is irrational, the evolution of the interface motion is not periodic. A non-zero γ indicates that the motion grows or decays according to the sign of γ. An irrational α yields a quasi-periodic evolution function. For the Faraday instability, it can be shown that α can only take two values: 0 and 1/2. As the imposed acceleration a is increased, one encounters regions in the (k, a) plane in which $\gamma > 0$ for one dominant temporal frequency, $j\omega/2$, where $j = 1, 2, 3 \ldots$ is an integer (see figure 3). Within each instability tongue, the amplitude of the mode grows exponentially. These tongues are called harmonic if $\alpha = 0$ and subharmonic if $\alpha = 1/2$. As k is increased, one encounters an alternating sequence of subharmonic and harmonic tongues, which are bounded by neutral curves $(k, a_c(k))$ on which $\gamma = 0$. On the neutral curves, the solutions are periodic:

$$\hat{\zeta}(k,t) = \sum_{n=-\infty}^{\infty} f_n(k) \mathrm{e}^{\mathrm{i}\left(n+\frac{1}{2}\right)\omega t}, \qquad \text{subharmonic case,} \tag{4.5a}$$

$$\hat{\zeta}(k,t) = \sum_{n=-\infty}^{\infty} f_n(k) \mathrm{e}^{\mathrm{i}n\omega t}, \qquad \text{harmonic case.} \tag{4.5b}$$

4.2. *Computation of the neutral curves*

We first compare our numerically calculated instability thresholds with those found by Kumar & Tuckerman (1994) for the same parameter values. The physical parameters are $\rho_1 = 519.933\,\mathrm{kg\,m^{-3}}$ and $\mu_1 = 3.908 \times 10^{-5}\,\mathrm{Pa\,s}$ for the lower fluid and $\rho_2 = 415.667\,\mathrm{kg\,m^{-3}}$ and $\mu_2 = 3.124 \times 10^{-5}\,\mathrm{Pa\,s}$ for the upper fluid. The other parameters are $\sigma = 2.181 \times 10^{-6}\,\mathrm{N\,m^{-1}}$ and $g = 9.8066\,\mathrm{m\,s^{-2}}$. The frequency of the forcing is $\omega/2\pi = 100\,\mathrm{Hz}$ and thus its period is $T = 0.01\mathrm{s}$. The capillary length is defined as $l_c = \sqrt{\sigma/(|\rho_1 - \rho_2|g)}$. The container height is taken to be $5l_c = 0.231\,\mathrm{mm}$, and the interface, when unperturbed, is equidistant from the top and bottom boundaries. We consider several wavenumbers k and set the x dimension of the box in each case to one expected wavelength $\lambda = 2\pi/k$, i.e. to between 0.074 and 0.224 mm, as listed in table 1. We can estimate the importance of various physical effects for these parameters by defining dimensionless quantities with length k^{-1} and forcing period T. The Bond number $Bo = (kl_c)^{-2} = |\rho_1 - \rho_2|\, g/(\sigma k^2)$ measures the relative importance of gravitational to capillary effects and ranges between 0.0649

$k(\mathrm{mm}^{-1})$	$\lambda(\mathrm{mm})$	No. of gridpoints in x/z	a_c/g (Theor.)	a_c/g (Comp.)	Error(%)
28	0.224	124/128	4.375	4.407	0.7
32.5	0.193	96/128	3.777	3.800	0.6
35	0.180	100/128	3.960	3.954	−0.1
48	0.131	72/126	12.506	12.207	−2.4
60.9	0.103	56/126	19.760	19.922	0.8
85	0.074	48/144	41.953	42.358	1.0

TABLE 1. Comparison of the computed a_c with Floquet theory for various wavenumbers k.

and 0.598. The Reynolds number $Re = \rho/(\mu k^2 T)$ is a non-dimensional measure of viscous damping and ranges between 0.184 and 1.70 for both fluids.

We have computed the critical acceleration from our fluid-dynamical simulation for the wavenumbers listed in table 1. Initially, the interface is sinusoidal with wavevector $\boldsymbol{k}$ parallel to the x-axis and the velocity is zero. Moreover, to ensure that the solution corresponds initially to the linear solution, we require the amplitude of the interface displacement to be small compared to λ. In order to maintain a roughly cubic mesh and a minimum x-resolution of about 50 grid cells per wavelength, we vary the resolution in the z direction between 126 and 144 points. Since $\boldsymbol{k}$ points along the x direction, ζ does not depend on y (neither do the velocity nor the pressure) and so the size of the domain and resolution in y are arbitrary. The acceleration a is taken near $a_c(k)$, the expected critical acceleration corresponding to each wavenumber. At the threshold, the flow undergoes a pitchfork bifurcation. Since the growth rate is proportional to $a - a_c$ close to the neutral curve, it is sufficient to find the growth rates for two values of a and to interpolate linearly between these points.

In figure 3, we plot the values of a_c obtained from our fluid-dynamical simulation for several values of k, along with the curves $(k, a_c(k))$ obtained from the method of Kumar & Tuckerman (1994). Figure 3 shows that these thresholds are in good agreement, despite whatever inaccuracies in a_c are introduced by spatial discretization and linear interpolation. The relative error in the critical acceleration at the conditions previously stated is of the order of a few per cent as shown in table 1.

The results suggest that there is a k below which calculation of the growth rates is not possible. Some zones of the diagram are not accessible because a domain of width $2\pi/k$ necessarily accommodates all wavenumbers which are integer multiples of k up to the resolution limit $\pi/k\Delta x$. The coefficients of the Fourier expansion of the initial condition differ slightly from zero due to finite-difference spatial approximations and if the growth rate of one of these is greater than that of k itself, then it will quickly come to dominate k. This difficulty is exacerbated by the fact that several forcing periods are required for γ to stabilize. Then the amplitude, whose evolution was expected to be almost periodic, starts to rise before the precise determination of γ is possible, for example, in the range of k between 0 and roughly $15\,\mathrm{mm}^{-1}$. As we see in figure 3, the critical forcing is substantially lower for one of its multiples closer to $32.5\,\mathrm{mm}^{-1}$. The amplitude corresponding to this wavelength, although initially negligible, increases and rapidly dominates the mode we wish to study, making the calculation of γ unfeasible. In contrast, for $k = 48\,\mathrm{mm}^{-1}$, the growth rate did not vary significantly after having reached a value near zero (relative fluctuations of about 0.1 % of the growth rate's limit value were recorded after the stabilization).

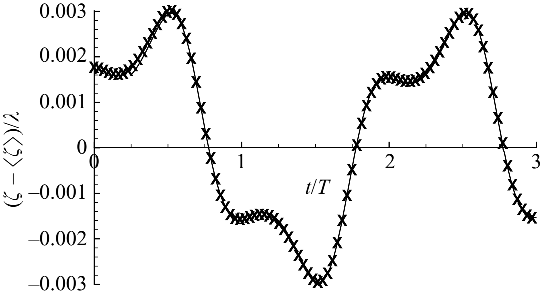

FIGURE 4. Linear evolution of the surface height deviation $\zeta(t) - \langle\zeta\rangle$ for $k = 48\,\text{mm}^{-1}$, in the first instability tongue. Our simulation results are plotted with symbols and those derived from a Floquet analysis with the solid line. The height and time are non-dimensionalized by the wavelength $\lambda = 2\pi/k$ and forcing period T, respectively.

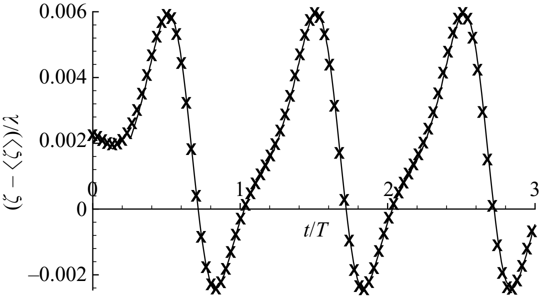

FIGURE 5. Linear evolution of the surface height deviation $\zeta(t) - \langle\zeta\rangle$ for $k = 60.9\,\text{mm}^{-1}$, in the second instability tongue. Same conventions used as figure 4.

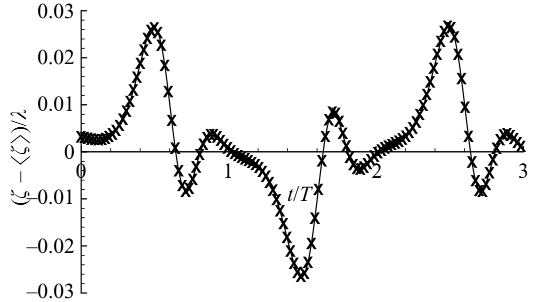

FIGURE 6. Linear evolution of the surface height deviation $\zeta(t) - \langle\zeta\rangle$ for $k = 85\,\text{mm}^{-1}$, in the third instability tongue. Same conventions used as figure 4.

4.3. *Temporal profile of a mode*

We recall from §4.1 that the time dependence of a Floquet mode is not sinusoidal. As a further validation, we can compare the results of our fluid-dynamical simulations to the entire temporal behaviour over a period. This is a stronger validation than merely predicting the threshold since it provides a comparison at every time instead of once per period.

In figures 4–6, we plot the deviation $\zeta - \langle\zeta\rangle$ from the flat interface as a function of time at a fixed spatial location from our fluid-dynamical simulation, for values $k = 48$, 60.9 and 85 mm belonging to the first three tongues. On the same figures, we plot the behaviour of (4.5), where the temporal coefficients $f_n(k)$ of the Floquet modes have been calculated by the method in Kumar & Tuckerman (1994). The value of a is set to the interpolated critical acceleration $a_c(k)$, so the oscillations approximately retain their initial amplitude as long as they remain small. The comparisons in figures 4–6 show a nearly perfect agreement. The differences observed initially, due to the phase difference between the initial conditions and acceleration, vanish remarkably quickly, in well under one period of oscillation of the container.

Figures 4–6 correspond to tongues $j\omega/2$, with $j = 1, 2, 3$, respectively, which show j zero crossings per forcing period T. Odd (even) values of j correspond to subharmonic (harmonic) oscillations, with period $2T$ (T). The temporal spectrum $f_n(k)$ becomes richer as k increases, leading to increasingly more complex modes, as can be observed by comparing figures 4–6. This strong anharmonicity of the curves is due to the increasing contribution of higher frequency trigonometric functions to the Floquet modes as a increases. The Floquet mode corresponding to $k_c = 32.5\,\mathrm{mm}^{-1}$, with the smallest value of $a = a_c$, should be closer to trigonometric, with a fundamental frequency of $\omega/2$.

5. Results: nonlinear analysis

In the full nonlinear evolution of the interface for $a > a_c$, the amplitude of the interface height grows in time until nonlinear terms in (2.2)–(2.7) become important. After that, the mode whose linear growth rate is maximal gives rise, via nonlinear resonances, to a series of other discrete modes, selected according to the magnitudes and orientations of their wavevector $\boldsymbol{k}$. This selection is responsible for the formation of patterns that will be the object of our further validations. We seek to compare our calculations with the experimental results of Kityk *et al.* (2005, 2009) where quantitative data concerning the Fourier spectrum $\hat{\zeta}(\boldsymbol{k}, t)$ are available for squares and hexagons.

We run our numerical simulations with the same experimental parameters as Kityk *et al.* (2005): $\omega/2\pi = 12\,\mathrm{Hz}$ $(T = 0.0833\,\mathrm{s})$, $\rho_1 = 1346\,\mathrm{kg\,m^{-3}}$, $\mu_1 = 7.2\,\mathrm{mPa\,s}$ for the lower fluid and $\rho_2 = 949\,\mathrm{kg\,m^{-3}}$, $\mu_2 = 20\,\mathrm{mPa\,s}$ for the upper fluid. The surface tension at the interface is $\sigma = 35\,\mathrm{mN\,m^{-1}}$, the total height of the vessel is 1.0 cm and the mean height of the interface, the initial fill height of the heavy fluid, is $\langle\zeta\rangle = 1.6\,\mathrm{mm}$ (with some uncertainty; see below). The Floquet analysis for these parameters yields a critical wavelength of $\lambda_c = 2\pi/k_c = 13.2\,\mathrm{mm}$ and a critical acceleration of $a_c = 25.8\,\mathrm{m\,s^{-2}}$. Here, the Bond number defined in §4.2 is $Bo = |\rho_1 - \rho_2|\,g/(\sigma k_c^2) = 0.49$. The Reynolds number $Re = \rho/(\mu k_c^2 T)$ is $Re_1 = 9.9$ and $Re_2 = 2.52$ for the lower and upper fluid, respectively.

Rather than starting from a sinusoidal interface, we chose to add two-dimensional white noise of small amplitude to $\langle\zeta\rangle$ to define the initial interface height $\zeta(x, y, t = 0)$ in order to excite every mode allowed by the box's horizontal dimensions and number of cells. It is thus possible to check that the correct critical mode (that whose growth rate is maximal) emerges from the linear dynamics. In order to reproduce the experimental results in a computational domain of a minimal size, the dimensions in x and y of the box must correspond to the periodicity and symmetries of the expected pattern. The minimal required resolution along these directions has been found to be between 40 and 50 cells per wavelength. The number of triangles used to represent the interface is 16 times the total number of horizontal gridpoints. The number of cells in the z direction is taken so that $\min_{S'} \zeta(x, y, t)$ is greater than about the height of 3–5 cells. The required vertical resolution thus varies with the forcing amplitude. The initial velocity is taken to be zero.

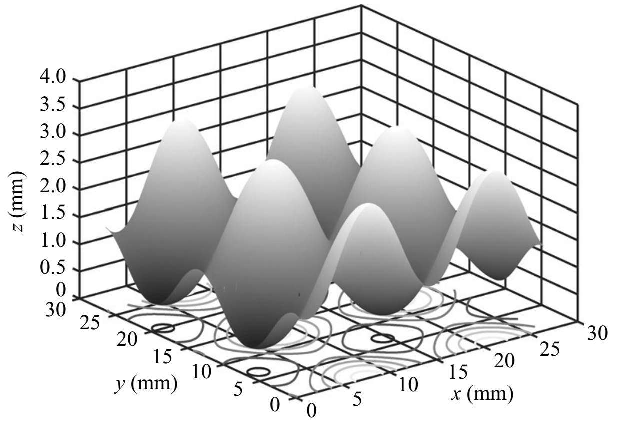

FIGURE 7. Example of square pattern. Height of interface as a function of the horizontal coordinates, at the instant corresponding to first arrow of figure 10, when height is maximal. Resolution in x, y, z directions: $80 \times 80 \times 160$. Note that the vertical scale is stretched with respect to the horizontal scale. Each horizontal direction in the figure is twice that of the calculation domain.

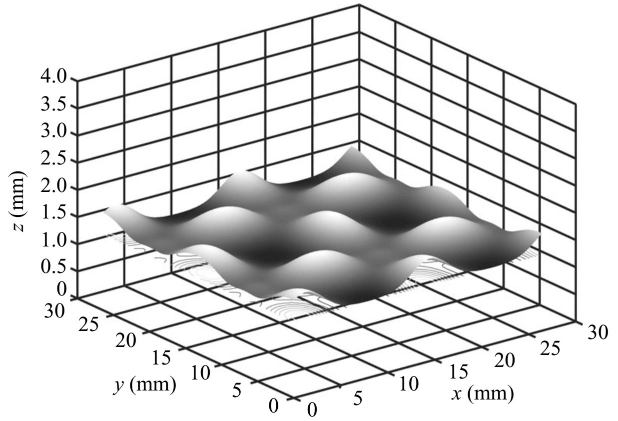

FIGURE 8. Example of square pattern, at the instant corresponding to second arrow of figure 10, time $0.24 \times 2T$ after figure 7.

5.1. *Square patterns*

To compare with the experiment of Kityk *et al.* (2005) for their square patterns, we choose the same forcing acceleration, $a = 30.0\,\mathrm{m\,s^{-2}}$. Our box has horizontal dimensions which we take both equal to $2\pi/k_c$. The time step is $\Delta t = 2.78 \times 10^{-4}$ s. Figures 7 and 8 represent examples of the patterns obtained at saturation under these conditions and are taken from the same simulation at the two instants shown by the two arrows in figure 10. The symmetries characterizing the squares (reflections and $\pi/2$ rotation invariance) are clear, showing a first qualitative agreement with Kityk *et al.* (2005) where both structures were observed. The pattern oscillates subharmonically, at $2T$, where T is the forcing period. Figure 7 is taken when the interface attains its maximum height, while figure 8 is taken at a time $0.24 \times 2T$ later. At this later time, we observe the dominance of a higher wavenumber, which will be discussed below.

Further quantitative investigations of the patterns involve the spatial Fourier transform of the interface height. In the case of square patterns, the distribution of the spatial modes is shown in figure 9. The modes with non-negligible amplitude

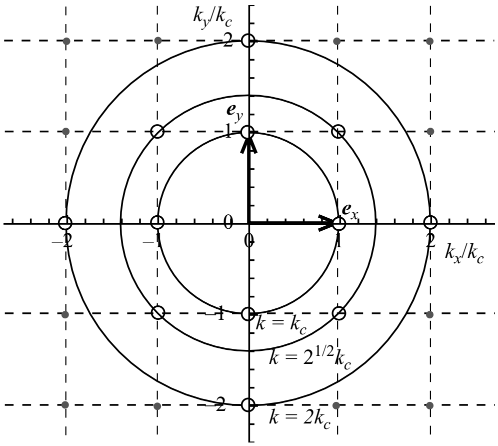

FIGURE 9. Lattice formed by the spatial modes comprising a square pattern. The principal modes, with wavenumbers k_c, $2k_c$ and $\sqrt{2}\,k_c$, whose evolution will be studied in figures 10 and 11 are indicated by hollow black circles.

are $\pm k_c\boldsymbol{e}_x$ and $\pm k_c\boldsymbol{e}_y$, with $|\boldsymbol{k}| = k_c$ and amplitude $A(k_c)$; $\pm 2k_c\boldsymbol{e}_x$ and $\pm 2k_c\boldsymbol{e}_y$, with $|\boldsymbol{k}| = 2k_c$ and amplitude $A(2k_c)$; and $k_c(\pm\boldsymbol{e}_x \pm \boldsymbol{e}_y)$, with $|\boldsymbol{k}| = \sqrt{2}k_c$ and amplitude $A(\sqrt{2}k_c)$. (For a square pattern, the amplitude of each mode is identical to that of each of its images through rotation by any integer multiple of $\pi/2$). The interface height is written as:

$$\zeta(\boldsymbol{x}, t) = \langle\zeta\rangle + A(k_c, t)\sum_{j=1}^{4} \mathrm{e}^{\mathrm{i}k_c\boldsymbol{e}_j\cdot\boldsymbol{x}} + A(2k_c, t)\sum_{j=1}^{4} \mathrm{e}^{\mathrm{i}2k_c\boldsymbol{e}_j\cdot\boldsymbol{x}}$$

$$+ A(\sqrt{2}k_c, t)\sum_{j=1}^{4} \mathrm{e}^{\mathrm{i}\sqrt{2}k_c\boldsymbol{e}'_j\cdot\boldsymbol{x}} + \text{higher order terms}, \qquad (5.1)$$

where $\boldsymbol{e}_j \equiv \boldsymbol{e}_x\cos(\pi j/2) + \boldsymbol{e}_y\sin(\pi j/2)$ and $\boldsymbol{e}'_j \equiv \boldsymbol{e}_x\cos(\pi/4 + \pi j/2) + \boldsymbol{e}_y\sin(\pi/4 + \pi j/2)$ for $j = 1, \ldots, 4$. We have chosen this notation, rather than $\hat{\zeta}(k, t)$ as used in (4.1), to facilitate comparison with Kityk *et al.* (2005, 2009).

We have compared the evolution of the three principal spatial modes (figure 10) and their temporal Fourier transform (figure 11) with the experimental results (Kityk *et al.* 2005). Here we turn the reader's attention to the recent erratum by Kityk et al. (2009) for correct quantitative comparisons of the spectra.

Figure 10 compares the experimental evolution of each spatial wavenumber to numerical calculations for two different mean heights $\langle\zeta\rangle = 1.6\,\mathrm{mm}$ and $\langle\zeta\rangle = 1.7\,\mathrm{mm}$. Our calculations show that the results depend strongly on $\langle\zeta\rangle$, which is the initial fill height of the heavy fluid. Our discussions with Kityk and Wagner (A. Kityk & C. Wagner, private communication, 2008) indicate that this is true as well in the experiments, and also that 0.1 mm is within the experimental uncertainty for their mean height. Thus we chose to vary $\langle\zeta\rangle$, in preference to other parameters, in order to check whether the range of amplitudes caused by experimental uncertainties includes those obtained numerically.

The main features found in Kityk *et al.* (2009) are recognized in figure 10. In particular, both the fundamental periodicity of each mode (harmonic or subharmonic) and the form of each numerical curve in figure 10 are very similar to the experimental data. The amplitudes and the phases are also quite close. Most of the experimental

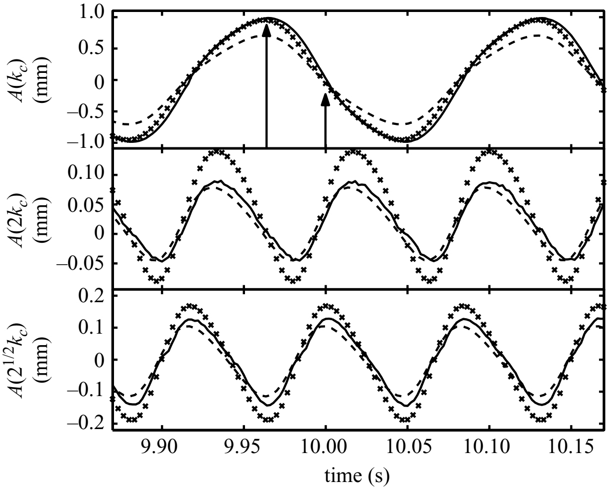

FIGURE 10. Temporal evolution of the amplitudes of the spatial modes with wavenumbers k_c, $2k_c$ and $\sqrt{2}k_c$. Solid curves represent the experimental results of Kityk *et al.* (2009), dashed curves and crosses represent numerical results for $\langle\zeta\rangle = 1.6$ mm and $\langle\zeta\rangle = 1.7$ mm, respectively. Resolution in x, y, z directions: $80 \times 80 \times 160$. Arrows, from left to right, show the time at which figures 7 and 8 have been plotted.

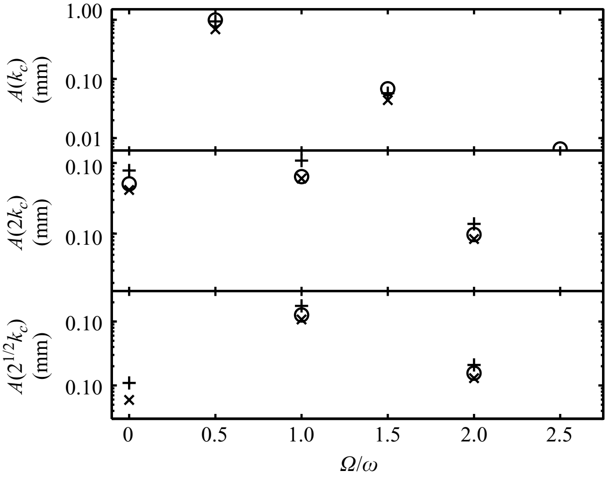

FIGURE 11. Temporal Fourier transform of the amplitudes in figure 10. Circles indicate experimental results of Kityk *et al.* (2009), while crosses and plus signs indicate numerical data with $\langle\zeta\rangle = 1.6$ mm and $\langle\zeta\rangle = 1.7$ mm, respectively.

amplitudes are bracketed by the numerical ones. Thus, they lie in the interval of amplitudes allowed by the range of uncertainties which is surely underestimated since only the uncertainty in $\langle\zeta\rangle$ has been taken into account. $A(k_c)$ crosses zero at times different from the two higher wavenumbers, $A(2k_c)$ and $A(\sqrt{2}k_c)$. At these instants, the higher wavenumbers dominate the pattern. In particular, the pattern of figure 8, taken near the second arrow in figure 10, when $A(k_c)$ is low, contains more peaks than that of figure 7, taken when $A(k_c)$ is high. The large ratio between the amplitude of k_c and the others makes this phenomenon very short-lived.

Figure 11 shows the temporal Fourier decomposition of the curves in figure 10. These spectra for the experiment Kityk *et al.* (2009) and for the computation are

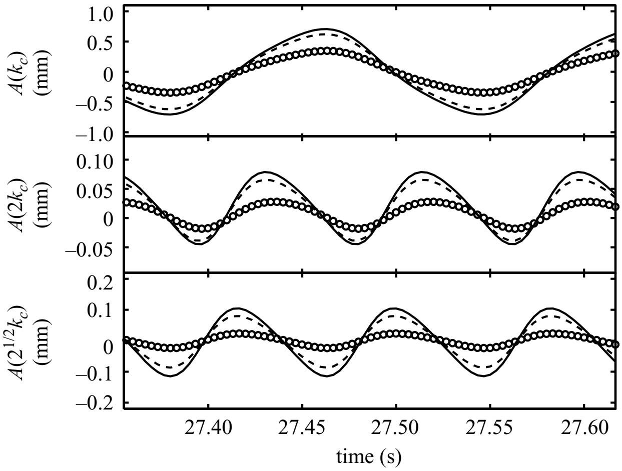

FIGURE 12. Temporal evolution of the amplitudes of the spatial modes with wavenumbers k_c, $2k_c$ and $\sqrt{2}k_c$ for square patterns. Study of the convergence with three different spatial resolutions. Circles indicate a resolution (in x, y, z directions) of $20 \times 20 \times 40$, dashed curves $40 \times 40 \times 80$ and continuous curves $80 \times 80 \times 160$. The time step is the same, $\Delta t = 2.78 \times 10^{-4}$ s, for all curves shown.

quite similar too. All of the square patterns that we have observed, once saturation is attained, remain so for the entire duration of the calculation.

We present a brief numerical grid convergence study in figure 12. All qualitative features, such as the square symmetry, were observed with each of the three resolutions chosen, despite the coarseness of the $20\times20\times40$ and $40\times40\times80$ grids. With increasing resolution, the principal spatial modes converge to the experimental curves shown in figure 10, with only a small difference between the curves with the two highest resolutions. The order of numerical convergence of the maximum and minimum of the amplitudes of each of the three modes in figure 12 shows that the convergence is between first and second order, which is expected to be the case with the immersed-boundary method. In particular, we would expect that a further doubling of the resolution would change the results by at most 4 % for the principal k_c mode.

5.2. *Hexagonal patterns*

When the amplitude of the forcing acceleration a is further increased, the modes can reorganize. The symmetries change and, in the experiments of Kityk *et al.* (2005), the initial square pattern becomes hexagonal. Though k_c remains constant, the horizontal dimensions of the minimal computational box necessary to support the periodic pattern must change too. These dimensions become $4\pi/k_c$ in y and $4\pi/(\sqrt{3}k_c)$ in x, as shown in figure 13. The wavevector lattice for hexagonal patterns is shown in figure 14. The principal modes are again of three amplitudes: k_c, $2k_c$ and $\sqrt{3}k_c$. When a pattern is hexagonal, a mode will have the same amplitude and temporal behaviour as each of its images through rotations by any integer multiple of $\pi/3$. The interface height is thus

$$\zeta(\boldsymbol{x},t) = \langle\zeta\rangle + A(k_c,t)\sum_{j=1}^{6} \mathrm{e}^{\mathrm{i}k_c\boldsymbol{e}_j\cdot\boldsymbol{x}} + A(2k_c,t)\sum_{j=1}^{6} \mathrm{e}^{\mathrm{i}2k_c\boldsymbol{e}_j\cdot\boldsymbol{x}} + A(\sqrt{3}k_c,t)\sum_{j=1}^{6} \mathrm{e}^{\mathrm{i}\sqrt{3}k_c\boldsymbol{e}'_j\cdot\boldsymbol{x}} + \text{higher order terms}, \quad (5.2)$$

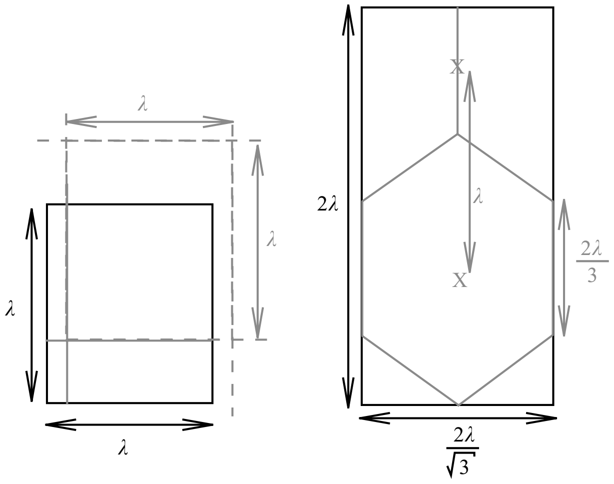

FIGURE 13. Boxes supporting the periodic patterns in the square and hexagonal cases. In black, the borders of the box. Light lines, pattern contained by each box; $\lambda = 2\pi/k_c$.

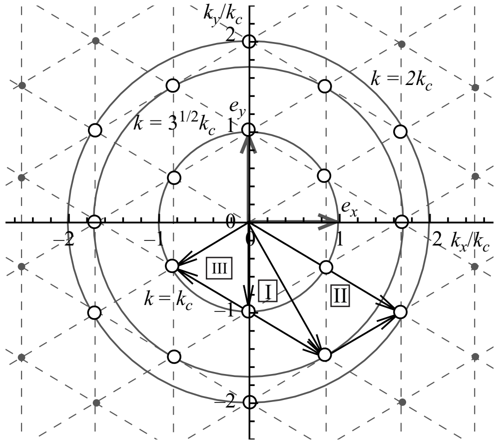

FIGURE 14. Lattice formed by the spatial modes comprising a hexagonal pattern. The principal modes, with wavenumbers k_c, $2k_c$ and $\sqrt{3}\,k_c$, involved in later quantitative investigations are indicated by hollow black circles. The labelled triangles illustrate resonance mechanisms leading to harmonic contributions to higher wavenumbers.

where $\boldsymbol{e}_j \equiv \boldsymbol{e}_x \cos(\pi j/3) + \boldsymbol{e}_y \sin(\pi j/3)$ and $\boldsymbol{e}'_j \equiv \boldsymbol{e}_x \cos(\pi/6 + \pi j/3) + \boldsymbol{e}_y \sin(\pi/6 + \pi j/3)$. for $j = 1, \ldots, 6$.

Our simulations are carried out at acceleration $a = 38.0\,\mathrm{m\,s^{-2}}$ and mean height $\langle\zeta\rangle = 1.6\,\mathrm{mm}$. We have used two different initial conditions: a rectangular pattern, and also white noise, as in our previous simulations of the square patterns. In both cases, hexagons emerge and saturate. The results shown below are those that emerge from the white noise. The time step varies during the calculation, depending on the viscous diffusion limit and the CFL. The spatial resolution is $58 \times 100 \times 180$ in the x, y, z, directions, respectively.

In figures 15–18, we show visualizations of the patterns at four instances in time. A movie of the temporal evolution of the hexagon pattern over one subharmonic oscillation is available in the online version of this article. The $\pi/3$

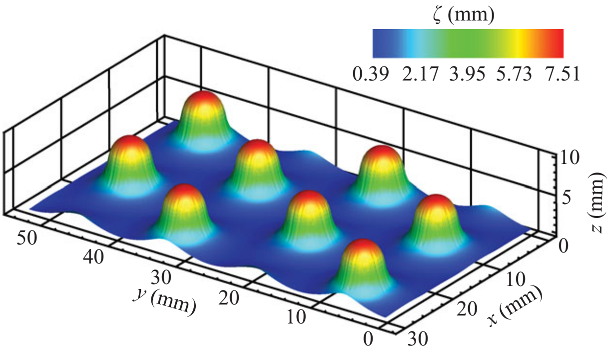

Figure 15. Snapshot of hexagonal pattern, taken when height of the interface peaks is maximal. Each horizontal direction is twice that of the calculation domain. A movie of the temporal evolution is available in the online version.

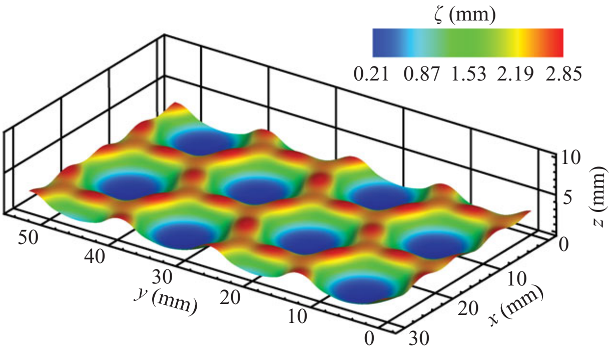

Figure 16. Snapshot of hexagonal pattern taken $t = 0.3 \times 2T$ after instant of maximal interface height.

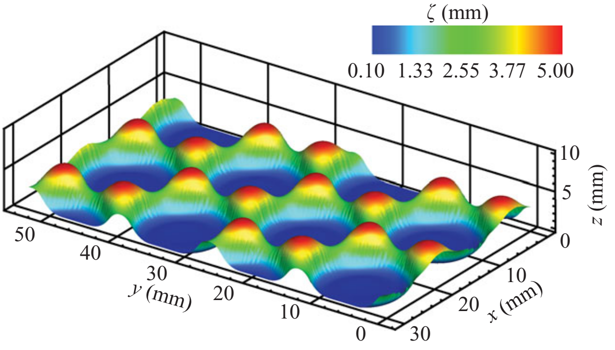

Figure 17. Snapshot of hexagonal pattern taken $t = 0.48 \times 2T$ after instant of maximal interface height.

rotational symmetry confirms that the rectangular numerical grid does not forbid the formation of hexagonal patterns, which are not aligned with this grid. The patterns reproduce several prominent features from the visual observations of hexagons in the experiments. For example, one can observe in figures 15 and 17 the up and down hexagons shown in the experimental snapshots (figure 10 of Kityk *et al.* 2005). The pattern in figure 18, when the surface elevation is minimal, is dominated by

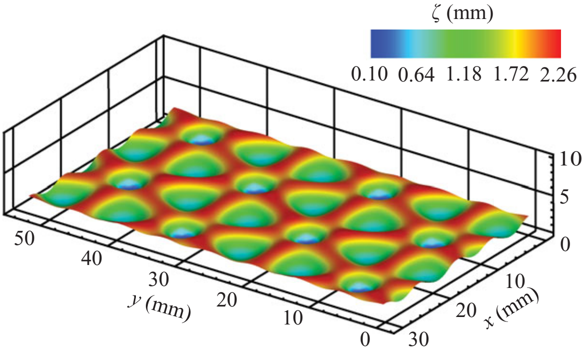

FIGURE 18. Snapshot of hexagonal pattern taken $t = 0.68 \times 2T$ after instant of maximal interface height.

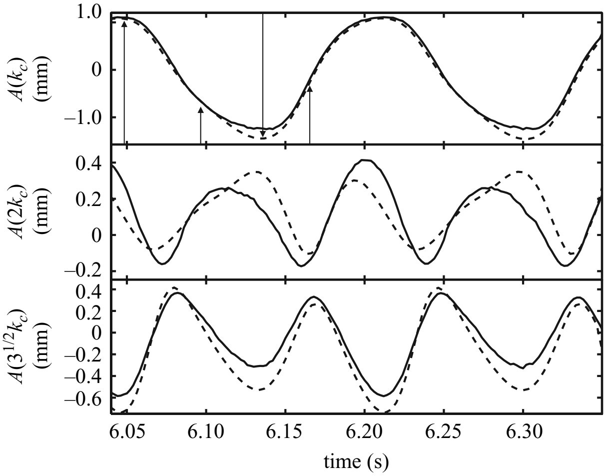

FIGURE 19. Temporal evolution of the amplitudes of the spatial modes with wavenumbers k_c, $2k_c$ and $\sqrt{3}k_c$. Solid curves represent experimental results (A. Kityk & C. Wagner, private communication, 2008) at $a \approx 38.5\,\mathrm{m\,s^{-2}}$. Dashed curves represent the simulation for $a = 38.0\,\mathrm{m\,s^{-2}}$ at resolution (in x, y, z directions) of $58 \times 100 \times 180$. Arrows indicate times corresponding to figures 15–18.

wavenumbers higher than k_c, as is also the case in figure 10 of Kityk *et al.* (2005). This is reflected by the disappearance of $A(k_c)$ and the resulting dominance of $A(2k_c)$ and $A(\sqrt{3}k_c)$ at the corresponding instant in the spectral timeseries of figure 19. This apparent wavenumber increase is analogous to that which occurs for the squares, shown in figures 8 and 10.

The spectra from experiments and simulations are represented in figures 19 and 20. Given that experimental uncertainties concerning the hexagons are greater than for the squares (A. Kityk & C. Wagner, private communication, 2008), the agreement is remarkable. The principal mode is well reproduced while the other two modes show rough agreement. It is striking that, in contrast to square patterns, every wavevector is a superposition of harmonic and subharmonic temporal modes, so that each has temporal period $2T$. This phenomenon was explained by Kityk *et al.* (2005) as a spatio-temporal resonance as follows. In the case of the square lattice, two

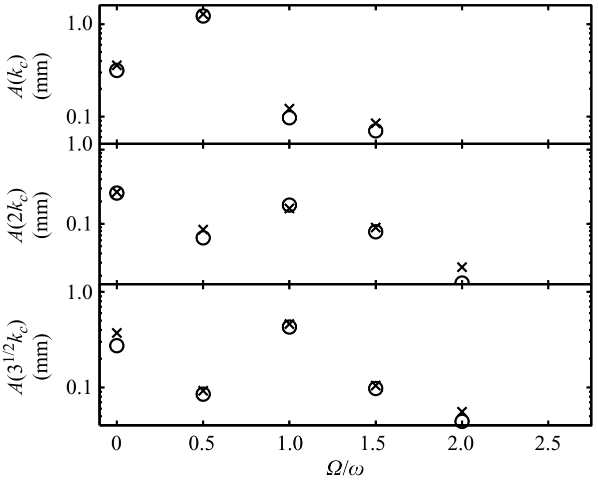

FIGURE 20. Temporal Fourier transform of the amplitudes in figure 19. Circles represent experimental results (A. Kityk & C. Wagner, private communication, 2008) for $a \approx 38.5\,\mathrm{m\,s^{-2}}$. Crosses represent numerical results for $a = 38.0\,\mathrm{m\,s^{-2}}$ at resolution $58 \times 100 \times 180$.

critical subharmonic modes (e.g. $k_c\boldsymbol{e}_x$ and $k_c\boldsymbol{e}_y$) interact to yield a higher wavenumber harmonic mode (e.g. $k_c(\boldsymbol{e}_x + \boldsymbol{e}_y)$). In the hexagonal case, two critical subharmonic modes (e.g. $-k_c\boldsymbol{e}_y$ and $k_c(\sqrt{3}\boldsymbol{e}_x - \boldsymbol{e}_y)/2$) interact to yield a higher wavenumber harmonic mode ($k_c(\sqrt{3}\boldsymbol{e}_x - 3\boldsymbol{e}_y)/2$), as in triangle I of figure 14. Further interaction of this mode with a critical subharmonic mode ($k_c(\sqrt{3}\boldsymbol{e}_x + \boldsymbol{e}_y)/2$) yields subharmonic contributions to the higher spatial wavenumber mode ($k_c(\sqrt{3}\boldsymbol{e}_x - \boldsymbol{e}_y)$), as shown in triangle II. Other quadratic interactions between critical subharmonic modes can contribute to a third harmonic mode of wavenumber k_c (triangle III).

In addition to the interface height, our simulations also produce the entire velocity field, which is the focus of figures 21–23. These figures show the velocity fields on horizontal planes at three instants spanning the oscillation period of a hexagonal pattern, as well as the vertical velocity on the interface. Figures 21, 22 and 23 correspond approximately to the visualizations of figures 15, 16 and 18, where the structures are more visible since the interface has been repeated periodically in the horizontal directions for clarity. The parameters are the same as those given previously, except that the acceleration a has been decreased to $36.0\,\mathrm{m\,s^{-2}}$, and the number of triangles used to represent the interface has been increased to 64 times the total number of horizontal gridpoints.

Figure 21 is taken at $t = 0.07 \times (2T)$, just after the interface reaches its maximum height (at $t = 0$), when the peaks are beginning to descend. Consequently, the fluid converges horizontally towards the interface peaks, then descends dramatically below them. The fluid then diverges horizontally outwards near the bottom and moves upwards in the large regions between the peaks. The motion shown in figure 22, at $t = 0.41 \times (2T)$, is quite different from that in figure 21. The peaks of figure 21 have collapsed into wide flat craters. The fluid converges inwards horizontally above the peaks, then descends into the craters and diverges outwards horizontally just below them. Figure 23, at $t = 0.73 \times (2T)$, shows that the rims of the wide flat craters seen in figure 22 have in turn collapsed inwards, forming circular waves which invade the craters, whose remnants are visible as dimples. The velocity field of figure 23 shows

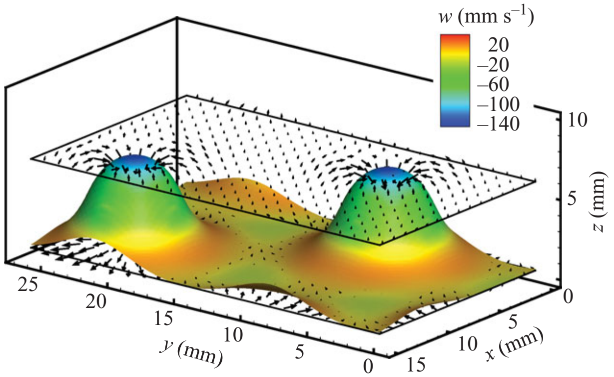

FIGURE 21. Velocity field at time $t = 0.07 \times (2T)$ after the instant of maximum height. Interface is coloured according to the vertical velocity w. Arrows show velocity field at $z = 0.53$ mm and $z = 6.08$ mm. (Total height is 10 mm, average interface height is 1.6 mm.) For clarity, velocity vectors are plotted only at every fourth gridpoint in each direction. Note that the vertical and horizontal scales are different. One computational domain is shown.

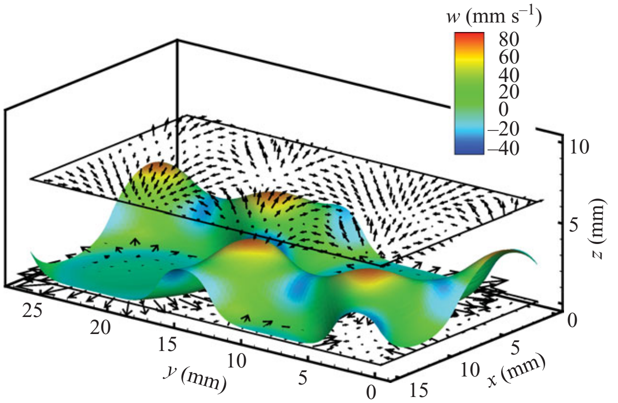

FIGURE 22. Velocity field at time $t = 0.41 \times (2T)$ after the instant of maximum height. Vectors shown at $z = 0.083$ mm and $z = 6.25$ mm. Vector and colour scales differ from those of figure 21.

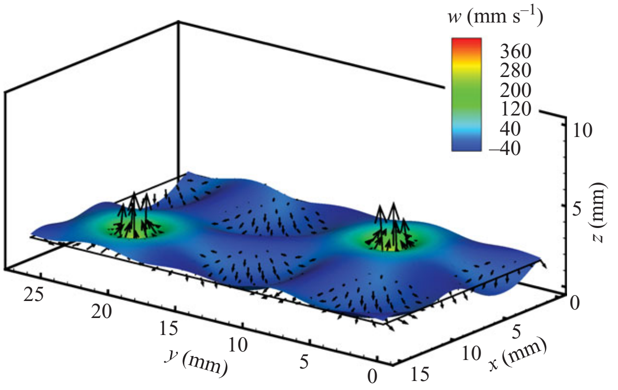

FIGURE 23. Velocity field at time $t = 0.73 \times (2T)$ after the instant of maximum height. Arrows show velocity field at $z = 1.58$ mm. Vector and colour scales differ from those of figures 21 and 22.

fluid converging horizontally below these dimples. These are erupting at velocities which are the largest in the cycle, and will eventually reconstitute the high peaks seen in figure 21.

Figures 21–23, as well as figures 15–18, show that these cases pose great computational difficulties. The interface periodically forms a very thin film (approximately 0.1 mm; see wide crater in figures 17 and 22) over large portions of the lower boundary, within which the velocity may be significant. These features make it difficult to adequately resolve the flow in this layer. For the time being we use a uniform grid spacing; however, in this case an adaptive grid would be more efficient and is under development. We have also simulated hexagons with resolutions of $70 \times 120 \times 100$ and $70 \times 120 \times 50$. Although we do not show these, the two highest resolutions lead to very similar spatial spectra with a maximum difference in amplitudes of the principal modes of about 5 % between the $70 \times 120 \times 100$ and $58 \times 100 \times 180$ resolutions. The case resolved by only 50 cells in the z direction shows differences mainly in the $2k_c$ mode where the difference between the $70 \times 120 \times 50$ and $58 \times 100 \times 180$ resolution is about 25 %; for the two other modes the difference is about 10 %. Hexagonal motifs were observed for all of the resolutions.

The calculation for the hexagon case, for the resolution of $58 \times 100 \times 180$ takes about 7 h per subharmonic oscillation on a 2.16 GHz Intel processor. This corresponds to 42 h of calculation time for 1 s of physical time.

In contrast to the square patterns, all of the hexagonal patterns that we have observed are transient. In our calculations, they last for several seconds, i.e. about 15–20 subharmonic oscillation periods, over which time the amplitudes and periods of the principal modes remain constant. This is also the case for the experimental observations (A. Kityk & C. Wagner, private communication, 2008), although the experimental lifetimes are longer. In our simulations, hexagonal patterns alternated with patterns with other symmetries, whose lifetimes were long (on the order of several seconds) but irregular. This behaviour suggests that the hexagonal state may belong to a heteroclinic orbit. A more extensive examination of the hexagonal regime will be the subject of a future investigation.

6. Conclusion

We have carried out full nonlinear three-dimensional simulations of Faraday waves. The incompressible Navier–Stokes equations for two fluid layers of different densities and viscosities are solved using a finite-difference method. The interface motion and surface tension are treated using a front-tracking/immersed-boundary technique. The simulations are validated in several ways. First, for small oscillation amplitudes, our computations match the solution of Kumar & Tuckerman (1994) to the Floquet problem which results from the linearized evolution equations. The boundaries of the instability tongues, i.e. the critical amplitude as a function of horizontal wavenumber are calculated for several wavenumbers on several tongues and are in good agreement with the theoretical values. The temporal dependence of the Floquet modes is also well reproduced by our numerical results, an even more quantitatively significant validation.

For finite oscillation amplitude, our computations reproduce the square and hexagonal patterns observed by Kityk *et al.* (2005, 2009) at moderate and high-oscillation amplitudes, respectively. Although the domains shown in figure 13 were chosen to accommodate square and hexagonal patterns respectively, we consider the emergence of these patterns at the appropriate parameter values a non-trivial test of our program, since these domains can also accommodate rectangles and stripes. Quantitative comparisons were made between experiment and simulation of the spatio-temporal spectra. Our numerical results lie well within the experimental uncertainty. The hexagonal patterns are long-lived transients and show intriguing dynamical behaviour. Our direct numerical simulations provide velocity fields and pressure throughout the entire domain of calculation. Thus, we have been able to ascertain precisely the fluid motion for the Faraday waves, both above and below the interface between the two fluids.

Our future studies of Faraday waves will include a more detailed investigation of the dynamics of the hexagonal patterns, and the simulation and interpretation of oscillons.

The authors acknowledge J. Fineberg, E. Knobloch and A. Rucklidge for insights on theoretical aspects of the Faraday phenomenon, J. Chergui, M. Firdaouss and K. Borońska for advice regarding implementation of certain numerical algorithms and, especially, A. Kityk and C. Wagner for extensive discussions and for sharing their experimental data.

REFERENCES

Bechhoefer, J., Ego, V., Manneville, S. & Johnson, B. 1995 An experimental study of the onset of parametrically pumped surface waves in viscous fluids. *J. Fluid. Mech.* **288**, 325–350.

Benjamin, T. B. & Ursell, F. 1954 The stability of the plane free surface of a liquid in vertical periodic motion. *Proc. R. Soc. Lond., Ser.* A **225**, 505–515.

Besson, T., Edwards, W. S. & Tuckerman, L. S. 1996 Two-frequency parametric excitation of surface waves. *Phys. Rev.* E **54**, 507–513.

Beyer, J. & Friedrich, R. 1995 Faraday instability: linear analysis for viscous fluids. *Phys. Rev.* E **51**, 1162–1168.

Binks, D., Westra, M.-T. & van der Water, W. 1997 Effect of depth on the pattern formation of Faraday waves. *Phys. Rev. Lett.* **79**, 5010–5013.

Brackbill, J. U., Kothe, D. B. & Zemach, C. 1992 A continuum method for modelling surface tension. *J. Comput. Phys.* **100**, 335–354.

Cerda, E. A. & Tirapegui, E. L. 1998 Faraday's instability in viscous fluid. *J. Fluid Mech.* **368**, 195–228.

Chen, P. 2002 Nonlinear wave dynamics in Faraday instabilities. *Phys.* Rev. *E* **65**, 036308.

Chen, P. & Viñals, J. 1999 Amplitude equation and pattern selection in Faraday waves. *Phys. Rev.* E **60**, 559–570.

Chen, P. & Wu, K.-A. 2000 Subcritical bifurcations and nonlinear balloons in Faraday waves. *Phys. Rev. Lett.* **85**, 3813–3816.

Chorin, A. J. 1968 Numerical simulation of the Navier–Stokes equations. *Math. Comput.* **22**, 745–762.

Christiansen, B., Alstrøm, P. & Levinsen, M. T. 1992 Ordered capillary-wave states: quasicrystals, hexagons, and radial waves. *Phys. Rev. Lett.* **68**, 2157–2160.

Edwards, W. S. & Fauve, S. 1994 Patterns and quasi-patterns in the Faraday experiment. *J. Fluid Mech.* **278**, 123–148.

Faraday, M. 1831 On a peculiar class of acoustical figures; and on certain forms assumed by groups of particles upon vibrating elastic surfaces. *Phil. Trans. R. Soc. Lond.* **121**, 299–340.

Goda, K. 1979 A multistep technique with implicit difference schemes for calculating two- or three-dimensional cavity flows. *J. Comput. Phys.* **30**, 76–95.

GUERMOND, J. L., MINEV, P. & SHEN, J. 2006 An overview of projection methods for incompressible flows. *Comput. Methods Appl. Mech. Engng* **195**, 6011–6045.

HARLOW, F. H. & WELCH, J. E. 1965 Numerical calculation of time dependent viscous incompressible flow of fluid with free surface. *Phys. Fluids* **8**, 2182.

HIRT, C. W. & NICHOLS, B. D. 1981 Volume of fluid (VOF) method for the dynamics of free boundaries. *J. Comput. Phys.* **39**, 201–225.

HUEPE. C., DING, Y., UMBANHOWAR, P. & SILBER, M. 2006 Forcing function control of Faraday wave instabilities in viscous shallow fluids. *Phys. Rev.* E **73**, 16310.

KITYK, A. V., EMBS, J., MENKHONOSHIN, V. V. & WAGNER, C. 2005 Spatiotemporal characterization of interfacial Faraday waves by means of a light absorption technique. *Phys. Rev.* E **72**, 036209.

KITYK, A. V., EMBS, J., MENKHONOSHIN, V. V. & WAGNER, C. 2009 Erratum: spatiotemporal characterization of interfacial Faraday waves by means of a light absorption technique [PRE 72, 036209 (2005)]. submitted *Phys. Rev.* E **79**, 029902 (E) (2009).

KUDROLLI, A. & GOLLUB, J. P. 1996 Patterns and spatiotemporal chaos in parametrically forced surface waves: a systematic survey at large aspect ratio. *Physica* D **97**, 133–154.

KUDROLLI, A., PIER, B. & GOLLUB, J. P. 1998 Superlattice patterns in surface waves. *Physica* D **123**, 99–111.

KUMAR, K. 1996 Linear theory of Faraday instability in viscous fluids. *Proc. R. Soc. Lond.* A **452**, 1113–1126.

KUMAR, K. & TUCKERMAN, L. S. 1994 Parametric instability of the interface between two fluids. *J. Fluid. Mech.* **279**, 49–68.

LIOUBASHEVSKI, O., ARBELL, H. & FINEBERG, J. 1996 Dissipative solitary states in driven surface waves. *Phys. Rev. Lett.* **76**, 3959–3962.

MÜLLER, H. W. 1993 Periodic triangular patterns in the Faraday experiment. *Phys. Rev. Lett.* **71**, 3287–3290.

MÜLLER, H. W., WITTMER, H., WAGNER, C., ALBERS, J. & KNORR, K. 1997 Analytic stability theory for Faraday waves and the observation of the harmonic surface response. *Phys. Rev. Lett.* **78**, 2357–2360.

MURAKAMI, Y. & CHIKANO, K. 2001 Two-dimensional direct numerical simulation of parametrically excited surface waves in viscous fluid. *Phys. Fluids* **13**, 65–74.

O'CONNOR, N. L. 2008 The complex spatiotemporal dynamics of a shallow fluid layer. Master's thesis, Virginia Polytechnic Institute and State University, Blacksburg, VA.

OSHER, S. & SETHIAN, J. 1988 Fronts propagating with curvature dependent speed: algorithms based on Hamilton–Jacobi formulations. *J. Comput. Phys.* **79**, 12–49.

PESKIN, C. S. 1977 Numerical analysis of blood flow in the heart. *J. Comput. Phys.* **25**, 220–252.

PORTER, J., TOPAZ, C. M. & SILBER, M. 2004 Pattern control via multi-frequency parametric forcing. *Phys. Rev. Lett.* **93**, 034502.

RAYLEIGH, LORD 1883*a* On maintained vibrations. *Phil. Mag.* **15**, 229–235. Reprinted in *Scientific Papers*, vol. 2, 1900, pp. 188–193. Cambridge.

RAYLEIGH, LORD 1883*b* On the crispations of fluid resting upon a vibrating support. *Phil. Mag.* **16**, 50–58. Reprinted in *Scientific Papers*, vol. 2, 1900, pp. 212–219. Cambridge.

RUCKLIDGE, A. M. & SILBER, M. 2009 Design of parametrically forced patterns and quasipatterns. *SIAM J. Appl. Dyn. Syst.* **8**, 298–347.

SAAD, Y. 1996 *Iterative Methods for Sparse Linear Systems*. SIAM Publishing.

SHU, C. W. & OSHER, S. 1989 Efficient implementation of essentially non-oscillatory shock capturing schemes, II. *J. Comput. Phys.* **83**, 32–78.

SKELDON, A. C. & GUIDOBONI, G. 2007 Pattern selection for Faraday waves in an incompressible viscous fluid. *SIAM J. Appl. Math.* **67**, 1064–1100.

SUSSMAN, M., FATEMI, E., SMEREKA, P. & OSHER, S. 1998 An improved level set method for incompressible two-phase flows. *Comput. Fluids* **27**, 663–680.

TEMAM, R. 1968 Une méthode d'approximation de la solution des équations de Navier–Stokes. *Bull. Soc. Math. France* **96**, 115–152.

TRYGGVASON, G., BUNNER, B., ESMAEELI, A., JURIC, D., AL-RAWAHI, N., TAUBER, W., HAN, J., NAS, S. & JAN, Y.-J. 2001 A front-tracking method for the computations of multiphase flow. *J. Comput. Phys.* **169**, 708–759.

UBAL, S., GIAVEDONI, M. D. & SAITA, F. A. 2003 A numerical analysis of the influence of the liquid depth on two-dimensional Faraday waves. *Phys. Fluids* **15**, 3099–3113.

VALHA, J., LEWIS J. S. & KUBIE, J. 2002 A numerical study of the behaviour of a gas–liquid interface subjected to periodic vertical motion. *Intl J. Numer. Meth. Fluids* **40**, 697–721.

VEGA, J. M., KNOBLOCH, E., MARTEL, C. 2001 Nearly inviscid Faraday waves in annular containers of moderately large aspect ratio. *Physica* D **154**, 313–336.

ZHANG, W. & VIÑALS, J. 1997 Pattern formation in weakly damped parametric surface waves. *J. Fluid Mech.* **336**, 301–330.